



Determination of the vertical distribution of in-cloud particle shape using SLDR mode 35-GHz scanning cloud radar

Audrey Teisseire¹, Patric Seifert¹, Alexander Myagkov², Johannes Bühl¹, and Martin Radenz¹

¹Leibniz Institute for Tropospheric Research, Permoserstraße 15, 04318 Leipzig, Germany

²RPG-Radiometer Physics GmbH, Werner-von-Siemens-Str. 4, 53340 Meckenheim, Germany

Correspondence: Audrey Teisseire (teisseire@tropos.de)

Abstract. In this study we present an approach that uses polarimetric variables from a scanning polarimetric cloud radar MIRA-35 in the 45° slanted linear depolarization (SLDR) configuration, to derive the vertical distribution of particle shape (VDPS) between top and base of mixed-phase cloud systems. The polarimetric parameter SLDR was selected for this study due to its strong sensitivity to shape and low sensitivity to the wobbling effect of particles at different antenna elevation angles. For the VDPS method, elevation scans from 90° to 30° elevation angle were deployed to estimate the vertical profile of the particle shape by means of the polarizability ratio, which is a measure of the density-weighted axis ratio. Results were obtained by retrieving the best fit between observed SLDR-vs-elevation dependencies and respective values simulated with a spheroid scattering model. The applicability of the new method is demonstrated by means of three case studies of isometric, columnar and oblate hydrometeor shapes, respectively, which were obtained from measurements at the Mediterranean site of Limassol, Cyprus. The identified hydrometeor shapes are demonstrated to fit well to the cloud and thermodynamic conditions which prevailed at the times of observations. Some observations reveal that in mixed-phased clouds ice particle shapes tend to evolve from a pristine columnar or dendritic state at cloud top toward a more isometric shape at cloud base. Either aggregation or riming processes contribute to this vertical change of microphysical properties. The new height-resolved identification of hydrometeor shape and the potential of the VDPS method to derive its vertical distribution are helpful tools to understand complex processes such as riming or aggregation, which occur particularly in mixed-phase clouds.

1 Introduction

In the troposphere, a rich variety of cloud types exists, which are formed by characteristic microphysical processes. The structure of clouds is in general determined by the complex interaction of water vapor, ice, liquid droplets, vertical air motion and aerosol particles, acting as cloud condensation nuclei (CCN) or ice nucleating particles (INP) (Morrison et al., 2012; Ansmann et al., 2019). While in warm clouds the collision-coalescence process is the primary process responsible for precipitation, the situation is more complicated in ice-containing clouds having temperatures between -40°C and 0°C . In this temperature range, the coexistence of supercooled liquid water and ice is possible. Thus, in these mixed-phase clouds multiple cloud microphysical processes are intertwined as they contain a three-phase colloidal system consisting of water vapor, ice particles and supercooled liquid droplets (Korolev et al., 2017). The initial partitioning between the ice and liquid water is determined by the



25 CCN and INP reservoir and represents the prevalent conditions for secondary ice formation processes, riming and aggregation (Solomon et al., 2018; Fan et al., 2017), which are greatly involved in the precipitation transition in mixed-phase clouds.

Observation of the hydrometeor habit is a possible way to study cloud formation and precipitation because particle shape can be considered a fingerprint of crucial processes, including crystal growth, evaporation rate, ice crystal fall speed, and cloud radiative properties (e.g., Avramov and Harrington, 2010). Shape allows to distinguish pristine ice crystals from hydrometeors which have grown via aggregation or riming processes and can be considered as a tracer of the different processes contributing to the evolution of a cloud system. The overall structure of ice crystals grown in air can be classified into plate-like and columnar shapes as a function of temperature between -40° and 0°C . Bühl et al. (2016) and Myagkov et al. (2016a) showed that primary ice formation dominates in thin layers of stratiform or mixed-phase clouds of a geometrical thickness $\leq 350\text{ m}$, as growth processes in these thin clouds are constrained (Fukuta and Takahashi, 1999). In such cloud systems and conditions of liquid water saturation, the shape of ice crystals is thus related directly to the environmental temperature (Myagkov et al., 2016b). However, further complexity can be expected when the cloud systems become deeper and when the thermodynamic structure is less well defined as in single-layer stratiform mixed-phase clouds. Techniques which allow detecting the hydrometeor shape have high potential to contribute additional capabilities for the monitoring of cloud systems, to expand the understanding of the involved microphysical properties, and to support the improvement of the representation of these processes in numerical models. A way to discriminate different hydrometeor populations is the separation of peaks in cloud radar Doppler spectra (Radenz et al., 2019; Kalesse et al., 2019) using observations of ground-based cloud radar. However, this technique is limited, e.g., with respect to atmospheric turbulence, which broadens the spectra and makes the detection and separation of peaks difficult or even impossible.

Polarimetric cloud radar techniques have been shown to be valuable tools for the qualitative detection of ice crystal shape. Matrosov et al. (2012) demonstrated an approach where they associated measurements of Slanted Linear Depolarization Ratio (SLDR) mode scanning cloud radar to visual observations of ice crystal habits during a precipitation event. While this study demonstrates well the relationship between SLDR signatures and particle shape, it did not yet allow to quantify the particle shape directly based on the measurements. Such an approach has been presented by Myagkov et al. (2016a), who succeeded in predicting the particle shape and orientation based on hybrid-mode scanning cloud radar observations by means of the two quantitative parameters polarizability ratio and degree of orientation, respectively. Myagkov et al. (2016a) have shown that existing backscattering models, assuming the spheroidal approximation of cloud scatters, can be applied to establish a link between a set of measured polarimetric variables and the polarizability ratio. Polarizability ratio is a parameter defined by the geometric aspect ratio of particles and their refractive index. For ice particles the refractive index is almost a linear function of their apparent ice density. Note, that it is not directly possible to infer the aspect ratio and the apparent ice density from the polarizability ratio. However, since the polarizability ratio depends on the aspect ratio and the apparent ice density, we suggest using it to track the evolution of the ice particles from pristine state to aggregates and rimed particles. Even though developed for SLDR mode and Simultaneous Transmit Simultaneous Receive (STSR, hybrid)-mode cloud radars, applicability of the shape and orientation estimation retrieval was originally demonstrated only for a STSR-mode scanning 35-GHz cloud radar,



based on observations of stratiform cloud layers during the one-month field campaign Analysis of Composition of Clouds with
60 Extended Polarization Techniques (ACCEPT, Myagkov et al. (2016a)).

The goal of this study is to derive the vertical distribution of particle shape in clouds using the spheroid scattering model developed by Myagkov et al. (2016a) for application to regular long-term observations of a SLDR-mode 35-GHz scanning cloud radar. We introduce a simplified and versatile version of the original STSR-mode approach by concentrating on the retrieval of the polarizability ratio, as we consider this parameter to be more relevant for the investigation of cloud microphysical
65 processes in comparison to the degree of orientation. By doing so, observations of SLDR are sufficient for the retrieval, enabling a broader field of application. This paper aims on demonstrating the ability of this new method, hereafter referred to Vertical Distribution of Particle Shape (VDPS) method, to derive particle shape using data with a newly configured SLDR-mode 35-GHz cloud radar which was deployed in the Cyprus Clouds Aerosols and pRecipitation Experiment (CyCARE, Ansmann et al. (2019)) field campaign located in Limassol, Cyprus. In Section 2, instrumentation and campaign setup will be described and the
70 VDPS method will be introduced in Section 3. An evaluation is presented in Section 4, where case studies showing isometric particles, columnar crystals and dendrites, respectively, will be discussed. In Section 5, we will elaborate on the advantages and limits of this new algorithm as well as possible future improvements.

2 Dataset

2.1 SLDR-mode 35-GHz cloud radar MIRA-35

75 The central instrument for the present study is a modified version of the 35-GHz cloud radar Mira-35, which is operated in SLDR-mode. MIRA-35 is a dual-polarization radar which emits linearly polarized radiation through the co-channel, while the returned signals are received in both the co- and cross-channels. The SLDR-mode cloud radar was implemented based on the conventional Linear Depolarization Ratio (LDR)-mode by 45° rotation of the antenna system around the emission direction. The properties of the standard LDR mode Mira-35 are elaborated in detail in Görsdorf et al. (2015). The technical characteristics of MIRA-35 used in the CyCARE campaign in Limassol, Cyprus, are detailed in the Table 1. Standard vertical-stare
80 LDR-mode allows only to discriminate between hydrometeors with an isometric intersection and with a columnar intersection (Bühl et al., 2016). I.e., aggregates cannot be separated from generally horizontally oriented dendritic particles in vertical-stare mode because their scattering intersections appear to be similar. In order to optimize the Mira-35 cloud radar for improved measurements of hydrometeor shape and orientation, two modifications were applied to the standard setup as it is described
85 by Görsdorf et al. (2015). First, the cloud radar was mounted onto a positioner platform which allows for a freely definable position of the radar within a half sphere given by 360° of azimuth and 180° of elevation. The second modification addresses a 45° rotation of the receiver antenna around the emission direction. This operation mode, in general defined as SLDR-mode, has specific advantages in studies of the intrinsic relationship between the polarimetric signature of the particle shape and radar elevation angle. In contrast to the standard LDR mode, variations in the orientation of hydrometeors only have small effects on
90 the measured SLDR (δ_s), even at low elevation angles (Matrosov, 1991). In turn, δ_s in vertical pointing mode (elevation = 90°) is similar to the LDR observed with standard Mira-35 systems. This behavior is also of advantage because it ensures direct



Table 1. Technical characteristics of MIRA-35 SLDR-mode cloud radar during the deployment in the CyCARE campaign in Limassol, Cyprus.

Parameters	Values
Pulse power	30 kW
Pulse length	208 ns
Pulse repetition frequency	7500 Hz
nFFT points	512
Number of range gates	498
Number of spectral averages	15
Integration time	1 s
Range resolution	31.18 m

comparability to other standard LDR-mode radars in vertical-pointing measurements. In the framework of the presented study, the radar was steered toward geographic south direction and performed range-height-indicator (RHI) scans from 90° (zenith pointing) to 150°, corresponding to 30° elevation over the horizon toward north direction. This notation of the elevation angle range will be used throughout this article and on the figure captions.

Figure 1 describes the setup of one scan cycle as it was applied in the measurements of the SLDR-mode MIRA-35, used in this study. Each scan cycle starts at minute 29 of each hour. Within 6.5 minutes, two RHI-scans from 90° to 150° and from 150° to 90° elevation angle and one Plan Position Indicator (PPI) scan at 75° elevation are performed. During the remaining 53.5 minutes of each measurement hour, vertical-stare observations (at 90° elevation angle) are performed to support standard retrievals, such as done within Cloudnet (Illingworth et al., 2007; Radenz et al., 2021) or as required for Doppler-spectra analysis techniques (Radenz et al., 2019; Bühl et al., 2019; Vogl et al., 2022; Schimmel et al., 2022). A limit of 150° elevation angle was established to avoid physical barriers like trees or buildings. It is also a reasonable compromise between required horizontal homogeneity and the intensity of the SLDR gradient produced by the observed hydrometeors. As the detailed procedure of data acquisition was depicted by Görsdorf et al. (2015) and Myagkov et al. (2016b), the determination of the polarimetric parameters required for this study is only briefly outlined below. The primary measurement parameters are thus the complex Doppler spectra received by the detectors in the co- and cross-channel with respect to the emitted polarization plane $\dot{S}_{co}(\omega_k)$ and $\dot{S}_{cx}(\omega_k)$, respectively, with ω_k being the Doppler frequency shift of each individual spectral component k . The herein presented VDPS method only considers the main peak of the detected Doppler spectrum. Thus, in a next step, each data point is screened for the spectral component ω_k^{\max} where $\dot{S}_{cx}(\omega_k)$ is maximal. The following parameters are then only calculated for the Doppler spectral bin ω_k^{\max} . The frequency dependency is thus omitted in the following and the polarimetric properties linear depolarization ratio SLDR (δ_s) and co-cross-correlation coefficient (ρ_s) in slanted mode can be derived as follows:

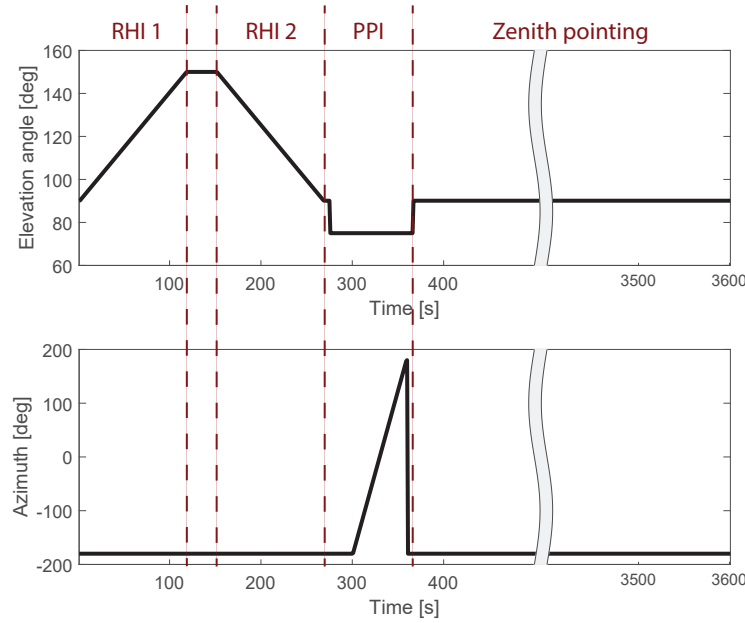


Figure 1. Depiction of the temporal evolution of elevation angle (top) and azimuth angle (bottom) during the hourly scan cycle of SLDR Mira-35 as applied during CyCARE. Red-colored dashed vertical lines denote the time periods of the different RHI (range-height indicator) and PPI (plane-position indicator) and zenith-pointing scan patterns.

$$\delta_s = \frac{\dot{S}_{cx} \dot{S}_{cx}^*}{\dot{S}_{co} \dot{S}_{co}^*} \quad (1)$$

$$\rho_s = \frac{|\langle \dot{S}_{co} \dot{S}_{cx} \rangle|}{(\langle \dot{S}_{co} \dot{S}_{co}^* \rangle \langle \dot{S}_{cx} \dot{S}_{cx}^* \rangle)^{1/2}} \quad (2)$$

115 where * is the complex conjugate.

The raw spectra of δ_s and ρ_s are subject to noise artifacts. Correspondingly, a noise filtering is performed to remove values which are below a given threshold value

$$n = m + 3\sigma \quad (3)$$

120 with m being the mean and σ being the standard deviation of noise in the cross channel. The properties of the noise in the cross channel we estimate from the last 5 range gates of each profile assuming no scattering is present. All data points of δ_s and ρ_s which are lower than n will be removed before any subsequent data analysis step is applied.

An important technical aspect which needs to be considered in the data analysis is the leakage of a fraction of signal from the co channel into the cross channel. This depolarization channel decoupling, in terms of the integrated cross-polarization



ratio (Chandrasekar and Keeler, 1993, ICPR), was found to be as low as -31 dB for the SLDR Mira-35 used in this study, as
125 was also confirmed in previous studies (Bühl et al., 2016; Radenz et al., 2021). The detection of $\delta_s < -31$ dB is therefore not
possible and entirely caused by the depolarization channel decoupling.

2.2 Dataset

MIRA-35 is operated as part of the Leipzig Aerosol and Cloud Remote Observations System (LACROS, Radenz et al. (2021)),
a suite of ground-based instruments of the Leibniz Institute for Tropospheric Research (TROPOS). Besides the SLDR-mode
130 Ka-band scanning cloud radar, LACROS comprises an extensive set of active and passive remote sensing instruments for the
characterization of aerosol properties, clouds, and precipitation, including multi-wavelength polarization lidar, Doppler lidar,
microwave radiometer and optical disdrometer. Data used in this study were acquired in the framework of a deployment of
LACROS at the Mediterranean site of Limassol, Cyprus (34.68° N, 33.04° E, 10 m a.s.l) during the Cyprus Aerosol and
pRecipitation Experiment (CyCARE, Ansmann et al. (2019); Radenz et al. (2021)). The region of Cyprus is a relevant location
135 for studies of the impact of aerosol on cloud processes because of a large variety of air pollutants, desert dust, and marine salt
particles in the atmosphere above the island. The CyCARE campaign was conducted from September 2016 until March 2018
and aimed on the determination of the relationship between aerosol properties and the formation of cirrus and mixed-phase
clouds (Ansmann et al., 2019; Radenz et al., 2021) in the heterogeneous freezing regime.

2.3 Measured and modeled δ_s and ρ_s

140 The VDPS method combines simulations of $\hat{\delta}_s$ and $\hat{\rho}_s$ assuming spheroidal particle shape with measurements of the same
two parameters of δ_s and ρ_s (see Section 3). Thereby and hereafter, the symbol $\hat{\cdot}$ denotes simulated parameters. In this study
we use the same set of analytical equations for the polarimetric variables as were derived in the previous study of Myagkov
et al. (2016b). The theoretical framework assumes Rayleigh scattering and utilizes a spheroidal approximation of particle
shape (Matrosov, 1991; Ryzhkov, 2001; Bringi and Chandrasekar, 2001). Parameters retrieved by the correlation of measured
145 δ_s and modeled $\hat{\delta}_s$ are the polarizability ratio (ξ) and the degree of orientation (κ) which describe the particles by means of
a density-weighted axis ratio and their preferred orientation, respectively. Figure 2 shows dependencies of $\hat{\delta}_s$ and $\hat{\rho}_s$ on the
polarizability ratio and degree of orientation of ice particles at 90° (zenith) and 150° (60° off-zenith) elevation angle. By
comparing Figures 2c and 2d, it can be seen that $\hat{\delta}_s$ is mostly sensitive to ξ (as noted by Matrosov et al. (2001)). In contrast, as
a comparison of Figures 2a and 2b shows, $\hat{\rho}_s$ is a proxy of degree of orientation κ (as described by Ryzhkov (2001)). Indeed,
150 $\hat{\rho}_s$ features no sensitivity with respect to ξ , as gradients of $\hat{\rho}_s$ against the elevation angle only exist with respect to κ . For our
radar configuration, the realistic range of possible polarizability ratios ξ spans from 0.3 to 2.3 giving an idea about the shape
of particles, while the degree of orientation κ , ranging from -1 to 1, describes the orientation of particles. κ will only be briefly
elaborated in this section as it will be used only qualitatively in the frame of this study. In the case of spheroidal approximation
and Rayleigh scattering regime, the polarizability ratio ξ , describing the shape of particles, is a function of permittivity and axis
155 ratio and is independent of the particle volume. A polarizability ratio $\xi = 1$ designates spherical particles or particles with low
density, while $\xi < 1$ and $\xi > 1$ describe oblate and prolate particles, respectively. Also for non-isometric particles, a decrease in

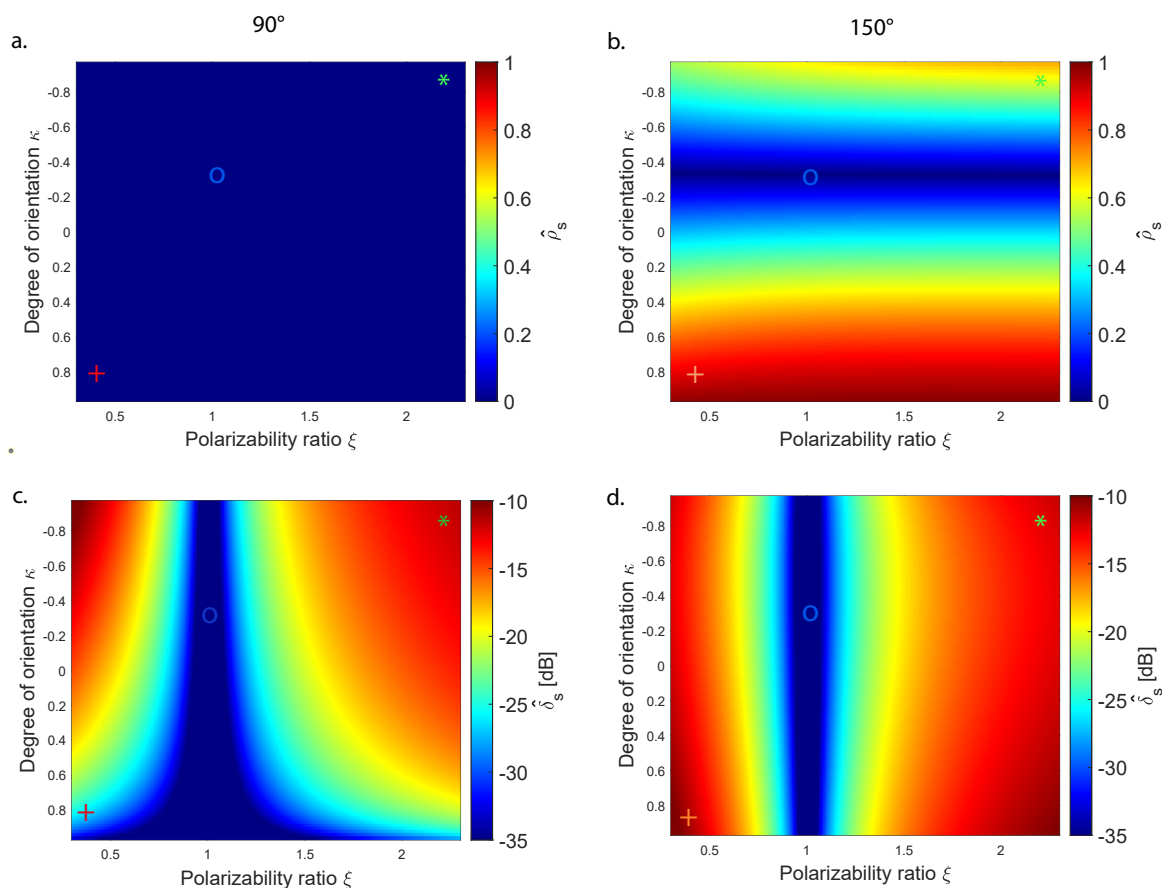


Figure 2. Modeled $\hat{\rho}_s$ (a,b) and $\hat{\delta}_s$ (c,d) as function of polarizability ratio ξ and degree of orientation κ for particles at $\theta = 90^\circ$ (a,c) and $\theta = 150^\circ$ (b,d) antenna elevation angle. The red '+' designs the oblate domain, the blue 'O', the isometric domain and the green '*' the prolate particle classes, respectively, when assuming a horizontally oriented main axis. The elevation dependency of these three scenarios are depicted further in Fig. 3

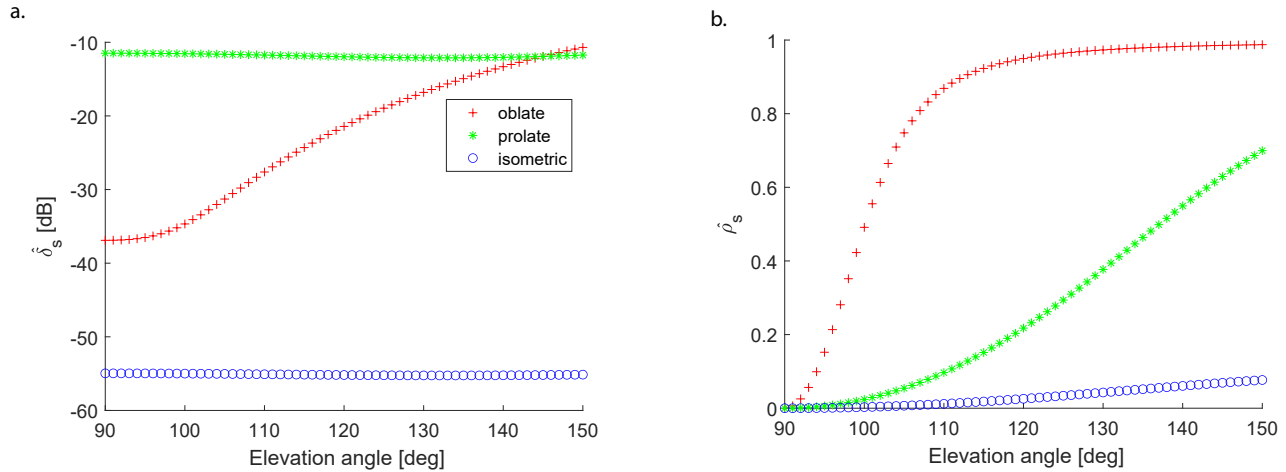


Figure 3. Modeled distributions of δ_s and ρ_s as a function of elevation angle between 90° to 150° for typical horizontally oriented oblate ("+" red), isometric ("o" blue), and prolate ("*" green) particles, respectively, issue from Figure 2.

apparent particle density causes ξ to approach a value of unity (Myagkov et al., 2016b). The degree of orientation characterizes the width of the particle orientation angle. For instance, $|\kappa| = 0$ corresponds to uniform distribution, while $|\kappa| = 1$ indicates that all particles are aligned in the same way. The sign of κ indicates the preferable orientation of the symmetry axis, i.e. $\kappa = +1$ indicates that all particles are aligned and have a vertical symmetry axis, $\kappa = -1$ corresponds to the case when particles have a predominantly horizontally aligned symmetry axis. We therefore assume $\kappa \geq 0$ for oblate particles and $\kappa \leq 0$ for prolate particles. Regarding Figures 2b and 2d we consider that $\kappa \approx -0.3$ is corresponding to randomly oriented isometric particles when $\rho_s \approx 0$ and δ_s is minimal and these values do not depend on the elevation angle.

As the goal of this paper is to derive the vertical distribution of particle shape in a cloud, which is mostly described by the polarizability ratio, this work concentrates on evaluating modeled vs. observed values of δ_s . The transition from modeled and measured δ_s and ρ_s is shown Figure 3 where the δ_s and ρ_s distribution are based on the model Figure 2. Indeed symbols "+", "o" and "*" represent oblate, isometric and prolate particles, respectively. This method is based on findings of Matrosov et al. (2012), who showed distinct elevation-dependent signatures of δ_s for particles with different shapes. As illustrated in Figure 3, oblate particles are characterized by a positive gradient of both δ_s and ρ_s from 90° to 150° elevation angle, while prolate particles are characterized by nearly constant and relatively high values of δ_s (around -20 dB for standard columns and -15 dB for pronounced needles of high axis ratio) and a positive gradient of ρ_s . Nearly spherical particles are described by a low gradient of both polarimetric parameters δ_s and ρ_s (Figure 3). Dendritic particles produce scattering similar to isometric particles when pointing to the zenith (90° elevation angle). But the dendrites, known to align predominantly horizontally along their planar planes, will increasingly appear oblate at a low elevation angle. That is why in the case of dendrites, δ_s , representative of the particle shape, is minimal at zenith pointing and increases until 150° elevation angle. ρ_s for horizontally aligned dendrites is expected to increase while scanning from 90° to 150° elevation angle. Indeed at zenith pointing dendrites have random orien-



tation in the polarization plane, while at a low elevation angle horizontally aligned particles produce rather coherent returns in both polarimetric channels. Finally, the isometric primary particle shape class containing droplets, aggregates and graupel is represented by constantly low values of δ_s and ρ_s at all angles between 90° and 150° elevation angle. Note, that it is not directly possible to classify the type of isometric particles (i.e. aggregate or rimed particle) since they have similar angular polarimetric signatures. Discrimination between these types of particles can be done e.g. using multiple-frequency observations (Kneifel et al. (2016)) but this is out of the scope of the current study. VDPS method aims to differentiate these three particle shape classes in order to determine microphysical processes occurring in mixed-phase clouds.

3 Methodology

The concept of the VDPS approach is to realize a tailored retrieval of the vertical distribution of particle shape. The VDPS method, adapted for the SLDR-mode scanning cloud radar as introduced in Section 2.1, has the particularity of combining simulated and measured values of δ_s at only the two elevation angles of 90° and 150° . Availability of a shape retrieval for only two elevation angles would allow much shorter scan cycles compared to the full RHI scans utilized in earlier studies such as of Myagkov et al. (2016b). As the VDPS method relies on polarimetric measurements at different elevation angles, horizontal homogeneity of the observed clouds is required. In this study, this prerequisite is achieved by means of a combination of experienced-eye evaluation of the obtained RHI scans and the requirement of a minimum number of data points in each layer, as will be explained in Section 3.1. The general flow chart describing the three-step procedure is depicted in Figure 4. Within the first step, presented in Section 3.1, the data is prepared for evaluation against a spheroid scattering model, presented in Section 3.2. By combination of this model with observations, the range of possible primary particle shape classes is identified and the associated uncertainties are assessed in Section 3.2. In the final step presented in Section 3.3, gradients calculated in Section 3.1 are deployed to identify only one possibility of the three general primary particle shape classes, in order to assign the proper polarizability ratio ξ and quantify the primary particle shape class determined in Section 3.2.

3.1 Construction of polarimetric gradients

For each of the four individual scan patterns described in Figure 2, the returned signals in the co- and cross-channel $\dot{S}_{co}(\omega_k)$ and $\dot{S}_{cx}(\omega_k)$ collected by MIRA-35 are saved in a level-0 file, in the pdm format defined by Metek company. Consequently, the pdm data are in a first step converted into NetCDF format containing the polarimetric measurements of $\delta_s(\omega_k)$ and $\rho_s(\omega_k)$, calculated with equations (1) and (2), respectively, as well as θ and range. Next, the noise filtering (equation (3)) is applied as explained in Section 2.3 and only the maximum spectral component of the remaining noise-free spectra are selected. Thus, arrays of δ_s and ρ_s are obtained which depend on time and range. All range values are converted into height above ground, using the elevation angle θ as additional input. A main loop is used to separate the observations into multiple vertical 'height' layers. In general, any arbitrary value of height resolution can be chosen. For the current study, each height step corresponds to the range resolution of MIRA-35 (31,18 m), similar to as was done by Myagkov et al. (2016b). The following procedure is performed for each height layer which contains at least 20 Doppler spectra of δ_s . The value of 20 points per layer represents

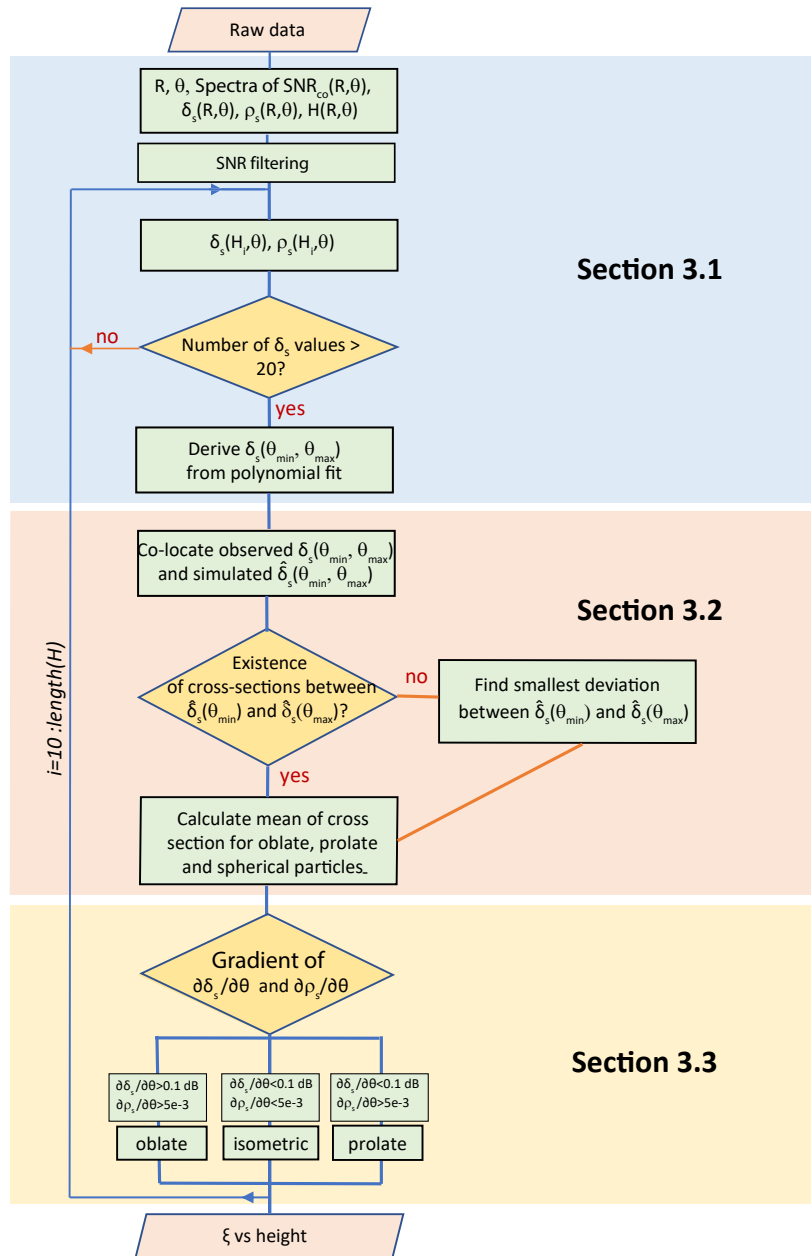


Figure 4. Flowchart describing the VDPS method.



about 15% of the maximal number of data points in one vector. If this limit is not reached, it could mean that no cloud was
210 detected at this layer or that not enough particles are contained at the investigated height level of the cloud layer, which will
influence the quality of results. In this situation, the procedure will be stopped only for this layer at this step (no results are
produced) and will continue to iterate into the next layer. If a sufficient amount of data points was found at a height level, new
vectors of $\delta_s(H, \theta)$ and $\rho_s(H, \theta)$ are built.

As shown in Fig. 3 and as will be elaborated further in Section 3.3, polarimetric signatures of different particle shapes
215 are most visible when the elevation angle difference of the performed scans is large. For this reason, it is sufficient to use
values of the polarimetric parameters δ_s and ρ_s only at 90° and 150° elevation angle. The VDPS algorithm runs automatically
for each selected RHI scan. In order to be as efficient as possible, we will look for the data points of δ_s associated with the
smallest values of elevation angles (θ_{\min} , usually zenith-pointing) and those with the largest values of elevation angles (θ_{\max} ,
usually 150°). Thus, in a next step, fit values of measured δ_s at the minimum elevation angle θ_{\min} , ($\delta_s(\theta_{\min})$), and at maximum
220 elevation angle θ_{\max} , ($\delta_s(\theta_{\max})$), are calculated. These notations will be used further in Section 3.2. It can be seen in Figure
3, that the modeled slope of the derived curve is never straight for δ_s , and the more appropriate fit to calculate $\delta_s(\theta_{\min})$ and
 $\delta_s(\theta_{\max})$ for this case is to use a 3rd degree polynomial fit. As reminder, we focus only on the particle shape in this paper,
that is why we will only use the fit values of $\delta_s(\theta_{\min})$ and $\delta_s(\theta_{\max})$ which depends primarily on the particle shape, while
 ρ_s describes the orientation of particles (Section 3.2). $\delta_s(\theta_{\min})$ and $\delta_s(\theta_{\max})$ are saved and will be utilized for the evaluation
225 against the spheroidal scattering model as presented in Section 3.2, for the same elevation angles θ_{\min} and θ_{\max} . In parallel we
will calculate mean gradients $\frac{\partial \delta_s}{\partial \theta}$ and $\frac{\partial \rho_s}{\partial \theta}$ estimated with a linear regression. The derived linear gradients are used to define
the primary particle shape class, as will be described in Section 3.3.

3.2 Combination of modeled and measured polarimetric parameters

The second section of the VDPS retrieval is dedicated to the comparison of measured (Section 3.1) and modeled polarimetric
230 parameters (Section 2.3). The original model based on Myagkov et al. (2016b) predicts minimum values of $\hat{\delta}_s$ that cannot
be reached with the current radar technology. As explained Section 2.1, the detection of $\delta_s < -31$ dB is not possible. This
adaptation is visible in Figures 2c and 2d with the extended blue domain in the middle, representing for this case, the minimum
modeled $\hat{\delta}_s$ values around -30 dB. The lower sensitivity of our radar compared to the modeled values implies an increase
of imprecision concerning isometric particles or particles of low density ($\xi = 1$). The modeled distribution of $\hat{\delta}_s$ and $\hat{\rho}_s$ from
235 90° to 150° elevation angle for three exemplary particle habits from oblate, isometric, and prolate particle shape classes, are
illustrated in the earlier introduced Figure 3. This graphic represents the theoretical aspect of the expected gradient in these
three different primary particle shape classes, which can be reproduced with direct measurements of δ_s and ρ_s . The second part
of this subsection is dedicated to compare the modeled $\hat{\delta}_s$ with $\delta_s(\theta_{\min})$ and $\delta_s(\theta_{\max})$ from direct measurements, processed in
Section 3.1, at θ_{\min} and θ_{\max} (Figure 5). $\delta_s(\theta_{\min})$ and $\delta_s(\theta_{\max})$ are calculated from the 3rd order polynomial fit (ref Section
240 3.1) at θ_{\min} and θ_{\max} , respectively.

In order to consider potential measurement inaccuracies, the 95% prediction interval of the polynomial fit will be used to
determine the potential range of the intersection. The model is processed for θ_{\min} and θ_{\max} and the algorithm identifies isolines

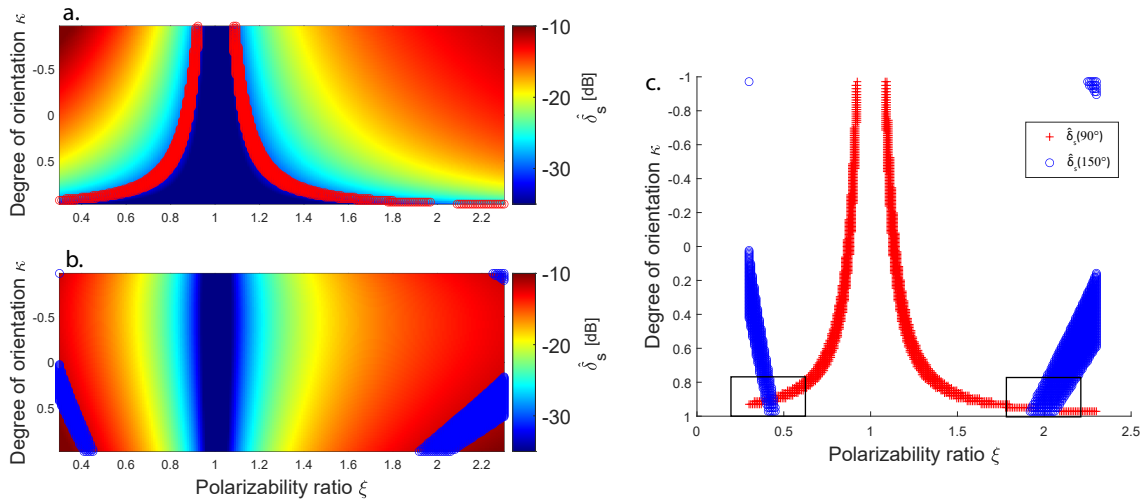


Figure 5. Determination of the possible values of ξ by searching for the intersections of observed δ_s in the data fields simulated with the spheroidal scattering model at (a) $\theta_{\min} = 90^\circ$ and (b) $\theta_{\max} = 150^\circ$ elevation angle. The red and blue curves in (a) and (b) depict the isolines of the observed values in the model space at 90° and 150° elevation, respectively. In (c) the overlay of the intersections of the isolines for 90° and 150° is shown. As observational input, hypothetical values of typical oblate particles with $\delta_s(\theta_{\min}) = -32dB$ and $\delta_s(\theta_{\max}) = -11dB$ were selected.

of $\delta_s(\theta_{\min}) \pm$ the 95% interval prediction, and $\delta_s(\theta_{\max}) \pm$ the 95% interval prediction, in the modeled fields of $\hat{\delta}_s$ at θ_{\min} and θ_{\max} , respectively, such as shown in Figure 5a and 5b. Intersections between $\hat{\delta}_s(\theta_{\min})$ and $\hat{\delta}_s(\theta_{\max})$ will appear in the model
 245 output (Figure 5c) and the associated values of ξ and κ are identified. If no intersection is found between $\hat{\delta}_s(\theta_{\min})$ and $\hat{\delta}_s(\theta_{\max})$,
 the algorithm searches for the point where the difference between $\hat{\delta}_s(\theta_{\min})$ and $\hat{\delta}_s(\theta_{\max})$ is the lowest. Finally, the algorithm
 characterizes the x-axis positions (polarizability ratio ξ) by deriving the mean and standard deviation of all overlapping data
 points included in each intersection (Figure 5). The values of ξ for each intersection are saved at each height iteration. In the
 final step, as described in Section 3.3, the appropriate particle shape class will be identified and the remaining, corresponding
 250 value of polarizability ratio will be attributed as solution.

3.3 Identification and quantification of particle shape classes

The processing steps conducted in Section 3.2 result in the provision of two intersections of $\hat{\delta}_s(\theta_{\min})$ and $\hat{\delta}_s(\theta_{\max})$, as is
 illustrated in Figure 5. Consequently, a possible solution for ξ exists for each primary particle shape class. The last step of the
 VDPS method is thus to identify the primary particle shape class among the possible solutions introduced in Section 3.2 and
 255 to quantify the primary class with the assigned value of ξ .

As introduced in Section 2.3, the relationship between δ_s , ρ_s and the elevation angle is an important aspect to determine
 the polarizability ratio ξ (Matrosov et al., 2012) and will be used in the following to discriminate between the primary shape



classes. Based on the comparison between the modeled and observed data from case studies representing the three particle shape classes, thresholds of $\frac{\partial \delta_s}{\partial \theta}$ and $\frac{\partial \rho_s}{\partial \theta}$ were determined in such a way that they allow for an unambiguous separation of the prolate, oblate and isometric hydrometeor shape classes. The resulting limit values were derived to be $lim_{\delta_s} = 0.1$ and $lim_{\rho_s} = 0.005$. The actual shape class selection criteria are summarized in Table 2 and are described in the following. If the slopes of $\frac{\partial \delta_s}{\partial \theta}$ and $\frac{\partial \rho_s}{\partial \theta}$ exceed lim_{δ_s} and lim_{ρ_s} , respectively, particles are assigned to the oblate primary particle shape class. If the slope of only $\frac{\partial \rho_s}{\partial \theta}$ exceeds lim_{ρ_s} and δ_s is relatively high, generally over -25 dB, but constant with a slope below lim_{ρ_s} , particles are assigned to the prolate primary particle shape class. If both gradients are below lim_{δ_s} and lim_{ρ_s} for both polarimetric parameters, particles are associated to the isometric primary particle shape class. If particles are assigned to the isometric particle shape class, ξ will be calculated with a mean of the associated values of ξ contained in both intersections of $\hat{\delta}_s(\theta_{min})$ and $\hat{\delta}_s(\theta_{max})$ on both sides of $\xi = 1$. In the oblate and prolate primary particle shape classes, the error bars are calculated based on the intersections of the standard deviation obtained for $\hat{\delta}_s(\theta_{min})$ and $\hat{\delta}_s(\theta_{max})$, following the same procedure as explained in Sections 3.2 and 3.3. Concerning the isometric primary particle shape class, ξ values of the two intersections identified before are used as error bars.

By putting the gradients of $\frac{\partial \delta_s}{\partial \theta}$ and $\frac{\partial \rho_s}{\partial \theta}$ into context to the shape-dependent limit numbers (lim_{δ_s} and lim_{ρ_s}), only one value of ξ is assigned to the previously identified primary particle shape class. Subsequently, the variability of the particle shapes in the selected primary particle shape class can be derived and applied to further data analysis steps. Figure 5 describes the comparison of the measured δ_s with $\hat{\delta}_s$ from the spheroidal scattering model using the VDPS method developed in Section 3.2. As an example a hypothetical case study where $\delta_s(\theta_{min}) = -32$ dB and $\delta_s(\theta_{max}) = -11$ dB was chosen, representing oblate particles like dendrites as depicted in Table 2. Regarding Figure 5b, we observe two intersections on both sides of $\xi=1$ and the choice of one of them requires an evaluation of the gradients of δ_s and ρ_s from θ_{min} to θ_{max} . The associated gradients of the hypothetical values of δ_s and ρ_s presented in Figure 6 confirm the assignment of ice particles in the primary oblate particle shape class due to the increase of both δ_s and ρ_s exceeding lim_{δ_s} and lim_{ρ_s} from θ_{min} to θ_{max} . The last step, according to the flow chart depicted in Figure 4, is to store the distribution of ξ previously calculated in Section 3.2 over the entire height of the cloud's profile. This distribution of particle shape delivers information about the stratification of ice particle shapes in a cloud which is a relevant indicator to understand in-cloud processes. The next section aims to evaluate and validate this new developed approach, the VDPS method, by means of three case studies, representing the three previously described particle shape classes prolate, oblate, and isometric.

4 Results

In this Section, we will demonstrate capabilities of the VDPS retrieval by means of three case studies associated with the three main particle shape classes isometric (rain, Section 4.1), prolate (columnar ice crystals, Section 4.2) and oblate (dendritic ice crystals, Section 4.3). The three case studies were selected from the CyCARE observations, presented in Section 2. Temperature provides an important constraint for the particle shape, since laboratory studies show a clear relationship between particle shape, temperature and supersaturation with respect to ice (Bailey and Hallett, 2009). Given conditions of liquid water saturation, near

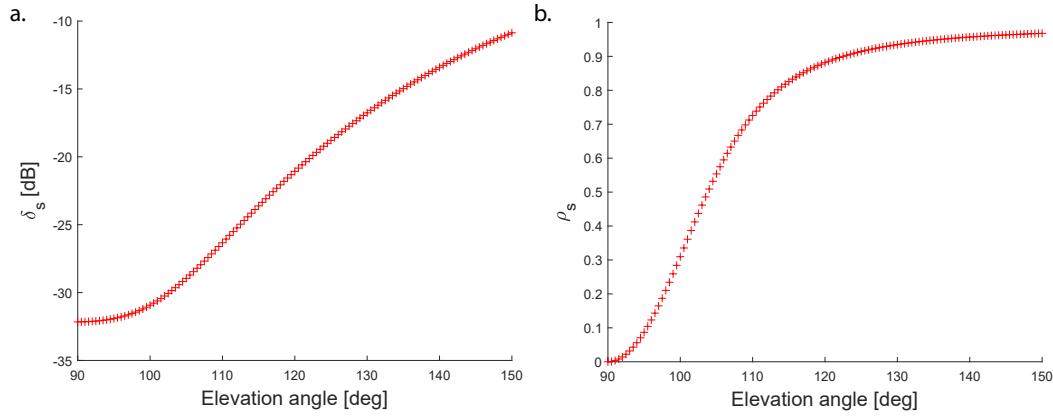


Figure 6. Gradient of (a) δ_s and (b) ρ_s as a function of elevation angle between $\theta_{\min} = 90^\circ$ and $\theta_{\max} = 150^\circ$ for the same hypothetical dendritic crystal population as presented in Fig. 5.

$T = -2^\circ\text{C}$, the growth is plate-like, near $T = -5^\circ\text{C}$ the growth is columnar, near $T = -15^\circ\text{C}$ the growth again becomes plate-like and at lower temperature, the growth becomes a mixture of thick plates and columns. A general meteorological situation is presented for each case study using the Cloudnet classification of targets based on MIRA-35 at zenith pointing and auxiliary instrumentation (Illingworth et al., 2007) and two RHI-scans of δ_s and ρ_s from θ_{\min} to θ_{\max} . Subsequently, the two polarimetric parameters δ_s and ρ_s measured at θ_{\min} and θ_{\max} are combined with the spheroid model introduced in Section 3.2. We will focus on the only one selected layer to illustrate the case studies even though all layers are processed to obtain the vertical distribution of particle shape. The last step aims to deliver insights in the quantification of the primary particle shape classes, as explained in Section 3.3, with the vertical distribution of ξ in the cloud. Since the proposed method uses the spheroidal approximation

Table 2. Assignment of the characteristic values of δ_s and ρ_s at $\theta_{\min} = 90^\circ$ and $\theta_{\max} = 150^\circ$ elevation angle and their gradients as function of θ . The associated typical ranges of ξ are given, as well. Please note, values of $\delta_s(\theta_{\min})$ and $\delta_s(\theta_{\max})$ for the isometric shape class correspond to the detection limit of SLDR (See Section 2). The limit values are $\lim_{\delta_s} = 0.1$ and $\lim_{\rho_s} = 0.005$

Shape class	Gradient	Value at 90°	Value at 150°	Polarizability ratio ξ
Oblate	$\frac{\partial \delta_s}{\partial \theta} > \lim_{\delta_s}$	$\delta_s(\theta_{\min}) = -30 \text{ dB}$	$\delta_s(\theta_{\max}) = -10 \text{ dB}$	$\xi = 0.2 - 0.8$
	$\frac{\partial \rho_s}{\partial \theta} > \lim_{\rho_s}$	$\rho_s(\theta_{\min}) = 0$	$\rho_s(\theta_{\max}) = 1$	
Isometric	$\frac{\partial \delta_s}{\partial \theta} < \lim_{\delta_s}$	$\delta_s(\theta_{\max}) = -31 \text{ dB}$	$\delta_s(\theta_{\min}) = -31 \text{ dB}$	$\xi = 0.8 - 1.2$
	$\frac{\partial \rho_s}{\partial \theta} < \lim_{\rho_s}$	$\rho_s(\theta_{\min}) = 0$	$\rho_s(\theta_{\max}) = 0.1$	
Prolate	$\frac{\partial \delta_s}{\partial \theta} < \lim_{\delta_s}$	$\delta_s(\theta_{\min}) = -20 \text{ dB}$	$\delta_s(\theta_{\max}) = -20 \text{ dB dB}$	$\xi = 1.2 - 2.4$
	$\frac{\partial \rho_s}{\partial \theta} > \lim_{\rho_s}$	$\rho_s(\theta_{\min}) = 0$	$\rho_s(\theta_{\max}) = 0.7$	

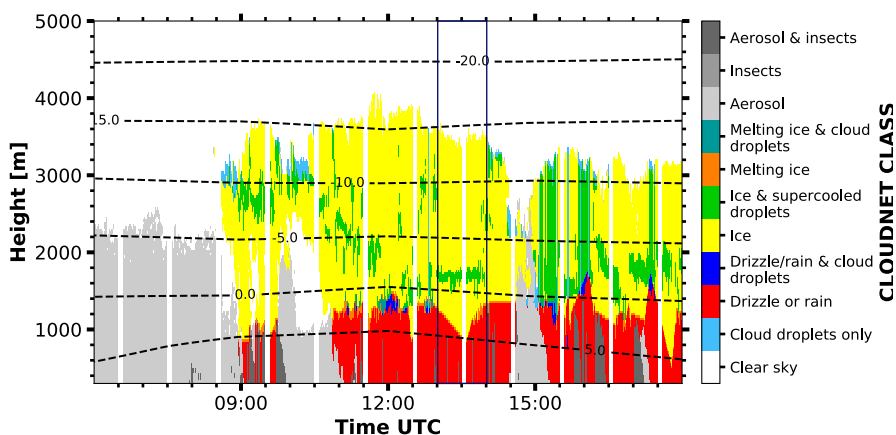


Figure 7. Cloudnet target classification mask as derived from observations at Limassol on 13 February 2017 from 08:00 to 16:00 UTC.

of pure-ice particles and assumes Rayleigh scattering, the derived ξ should be analyzed with care when the method applied
 300 to rain and melting layer. Since rain droplets corresponding to the maximum spectral line are often near spherical, ξ is valid
 since for spherical particles it is not strongly affected by the refractive index. In contrast, ξ in the melting layer is likely not
 valid, because the depolarization observed in the melting layer is not caused by columnar shapes of particles but by particle's
 strongly irregular shapes, water coating, and large size.

This Section aims to demonstrate that the VDPS method gives concordant results with the observations for the three primary
 305 particle shape classes, isometric, prolate and oblate particles, introduced in Section 3.2.

4.1 Isometric particle shape class: Rain event on 13 February 2017

The first case study concentrates on the occurrence of rain, i.e., hydrometeors representative for the primary isometric particle
 shape class. Measurements were recorded on 13 February 2017 at 13:31 UTC at Limassol. The studied cloud presented in the
 310 blue box of Figure 7, was identified to contain rain droplets at heights between 300 m to 1200 m. Above, a melting layer was
 present while further above ice particles were identified up to 4000 m height. The Cloudnet classification indicates a mixed
 phase layer at 1800 m height. We are particularly interested in the rain from 300 m to 1200 m height.

Figure 8a shows two RHI-scans of δ_s and ρ_s which were performed at 13:31 UTC. Values of δ_s from θ_{\min} to θ_{\max} are low
 (around -30 dB) and constant at heights below the melting layer. In Figures 8a and 8b, both δ_s and ρ_s are relatively constant
 from θ_{\min} to θ_{\max} , which is in agreement to what can be expected from scattering by isometric particles, as explained in
 315 Section 3.3. To illustrate this case study, we will focus only on one layer located at the height level from 868 m to 899 m,
 represented by the black line on the y-axis in Figure 8. In Figure 9b, the intersection of $\hat{\delta}_s(\theta_{\min})$ and $\hat{\delta}_s(\theta_{\max})$ is detectable by
 the red and blue curves which match the data of δ_s at θ_{\min} and θ_{\max} , respectively, with the spheroidal scattering model. We
 can distinctly notice the presence of two intersections between $\hat{\delta}_s(\theta_{\min})$ and $\hat{\delta}_s(\theta_{\max})$ from either side of the dashed red line,

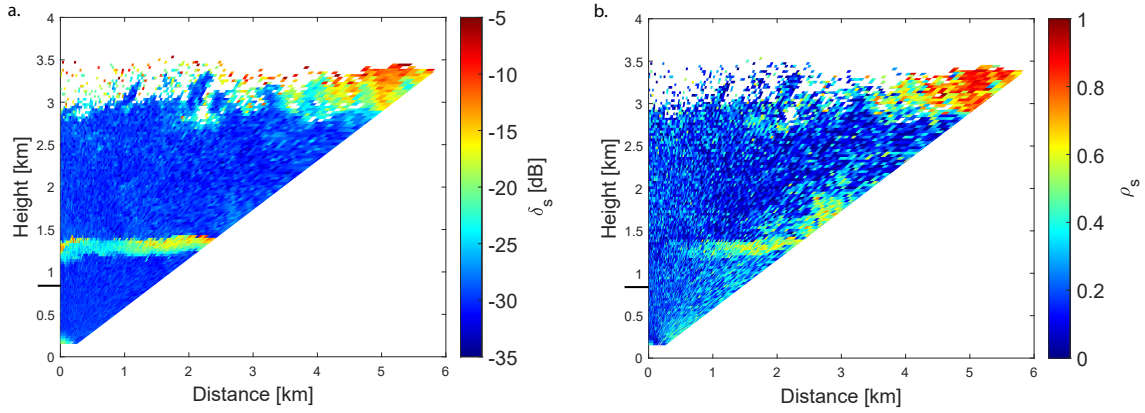


Figure 8. RHI-scans of (a) δ_s and (b) ρ_s observed on 13 February 2017, at 13:31 UTC in Limassol from 90° to 150° elevation angle. The black horizontal lines on the y axis mark the height of the analysed layer.

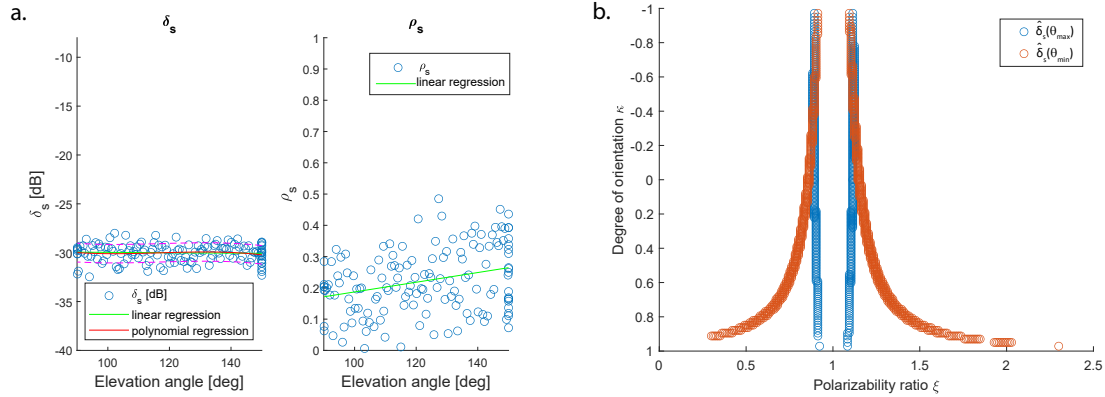


Figure 9. Detailed view into the isometric-shape case study presented in Figure 8 for the layer from 868 m to 899 m height. (a) Distribution of measured values of δ_s and ρ_s from θ_{\min} to θ_{\max} elevation angle and associated linear and polynomial fits. The dashed pink line in (a) corresponds to the 95% prediction interval from the third degrees polynomial function, used to determine the intersection of $\hat{\delta}_s(\theta_{\min})$ and $\hat{\delta}_s(\theta_{\max})$. (b) Intersection between $\hat{\delta}_s(\theta_{\min})$ and $\hat{\delta}_s(\theta_{\max})$ at θ_{\min} and θ_{\max} , respectively.

for $\xi = 0.9$ and $\xi = 1.1$. In Figure 9a, the gradient $\frac{\partial \delta_s}{\partial \theta}$ is constant from θ_{\min} to θ_{\max} where $\frac{\partial \delta_s}{\partial \theta} < \lim_{\delta_s}$ and, in Figure 9b, the
 320 gradient of ρ_s is weakly increasing from θ_{\min} to θ_{\max} where $\frac{\partial \rho_s}{\partial \theta} < \lim_{\rho_s}$. Regarding Table 2, this configuration describes the isometric primary particle shape class. Finally, the vertical distribution of ξ in the cloud is calculated following Section 3.3 and is shown in Figure 10.

Concerning the observations, the melting layer is well identified by a variable ξ , as explained in introduction of Section 4, in the height range from 1150 m to 1400 m height. Below this layer, ξ takes values around 1 which describes isometric

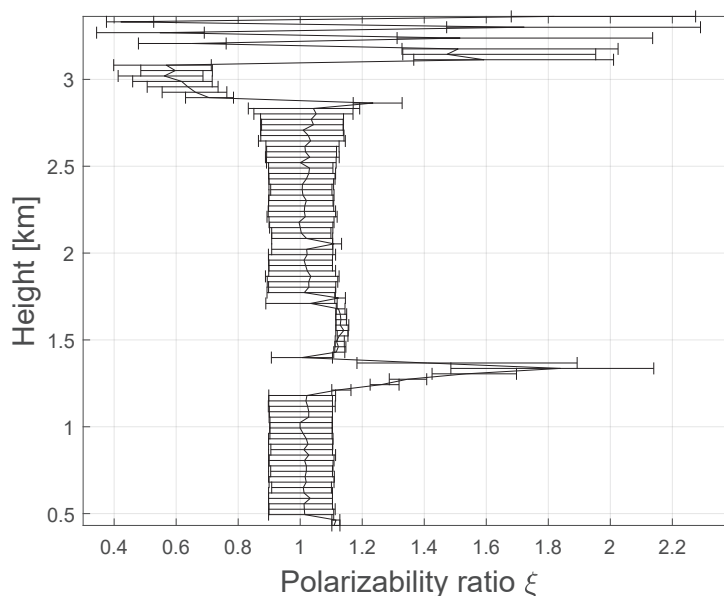


Figure 10. Vertical distribution of ξ as calculated with the VDPS method for each layer of the isometric-shape case study observed at Limassol, on 13 February 2017, 13:31 UTC.

325 particles (Section 3.2). Looking at the Cloudnet classification (Figure 7), the drizzle-or-rain class dominates the measurement at heights below approximately 1300 m. The melting layer at the transition between ice and rain is recognizable by elevated and scattered values of δ_s in Figure 8a. Figure 7 shows, in the blue box, a temperature higher than 0°C in this layer, which confirms the presence of liquid droplets, i.e., isometric particles. Application of the VDPS approach results in derivation of the same primary isometric particle shape class as determined based on the auxiliary observations (temperature and Cloudnet classification). Above the melting layer from 1700 m to 2800 m height, the VDPS method derived isometric particles, as well. Given that temperatures are below freezing level at these heights and that Cloudnet identified a mix of ice and supercooled droplets, it is likely that these isometric particles are the result of mixed-phase cloud processes, such as riming or aggregation, as both of which form isometric graupel particles or aggregates, respectively. Based on the VDPS method, the height level of the particle shape transition can be determined to be present at around 2800 m. Above, ξ was found to be well below 1, representing
 335 oblate particles, whose formation is also corroborated by the ambient temperatures of around -15°C . Applicability of the VDPS method is in the present case limited with respect to the interpretation of the microphysical process which led to the formation of the layer with isometric particle shape between approximately 1.5 and 2.7 km height. Doppler spectral methods or multi-frequency approaches could help here to investigate the possible contributions of riming and aggregation (Kneifel et al., 2016; Radenz et al., 2019; Kalesse-Los et al., 2022; Vogl et al., 2022).

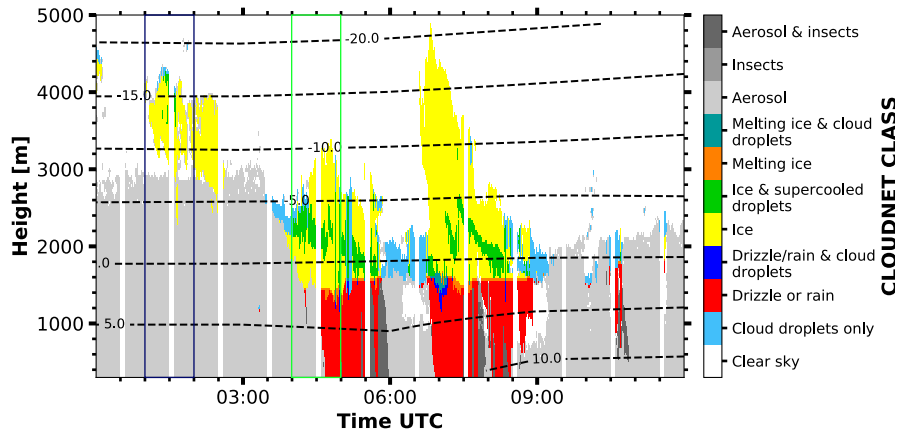


Figure 11. Cloudnet target classification mask as derived for observations at Limassol on 4 January 2017 from 00:00 to 12:00 UTC. The green and blue boxes denote the two scans that are discussed in further detail in Sections 4.2 and 4.3, respectively.

340 4.2 Prolate particle shape class: Columnar crystals on 4 January 2017 at 04:30 UTC

The second case study chosen to evaluate the VDPS method is dedicated to the characterization of columnar crystals. The corresponding measurement was recorded in Limassol on 4 January 2017 at 04:31 UTC. Figure 11 presents the Cloudnet classification for the time range from 00 to 12 UTC of 4 January 2017, with the selected case study marked by the green frame. Figure 12a shows the RHI scans of δ_s and ρ_s from 04:31 UTC. The rain event, which is shown after 0430 UTC in Fig 11 is not yet visible in the RHI scans. In turn, the melting layer is well recognizable at around 1450 m height. This melting layer is characterized by elevated values of δ_s of around -10 dB at all elevation angles from θ_{\min} to θ_{\max} . The onset of rain is barely visible by δ_s values which suddenly become very low (around -30 dB) below the melting layer, as is characteristic for isometric particles. Above the melting layer, the Cloudnet classification shows identified ice particles and a mixed-phase layer at around 2200 m height.

350 Above the melting layer, several ice-containing layers with different elevation-angle dependencies of δ_s can be distinguished. In the layer from 1900 m to 2400 m height, δ_s is around -15 dB. A second layer between 1500 m and 1900 m height is characterized by lower values of δ_s of around -20 dB. ρ_s increases from θ_{\min} to θ_{\max} while δ_s is constant. This constellation excludes isometric particles and oblate particles and is a specific property of columnar crystals (Table 2). As for the first case study, the retrieval is visualized only for one specific layer, which in this case spans from 1617 m to 1648 m height, indicated
 355 by the black line on the y-axis in Figure 12. Figure 13a shows $\frac{\partial \delta_s}{\partial \theta}$ and $\frac{\partial \rho_s}{\partial \theta}$ calculated with the linear regression function. These gradients of δ_s and ρ_s are such as $\frac{\partial \delta_s}{\partial \theta} < \lim_{\delta_s}$ and $\frac{\partial \rho_s}{\partial \theta} > \lim_{\rho_s}$. The 95% prediction interval is represented by the dashed pink line and is used at θ_{\min} to θ_{\max} to calculate $\delta_s(\theta_{\min})$ and $\delta_s(\theta_{\max})$, as elaborated in Section 3.2. In Figure 13b, once again two intersections of $\hat{\delta}_s(\theta_{\max})$ and $\hat{\delta}_s(\theta_{\min})$ exist for this layer. Considering the positive gradient of ρ_s and the constant behaviour of δ_s , we can identify the intersection in the columnar particle shape class with $\xi > 1$ and $\kappa < -0.8$ as the correct one.

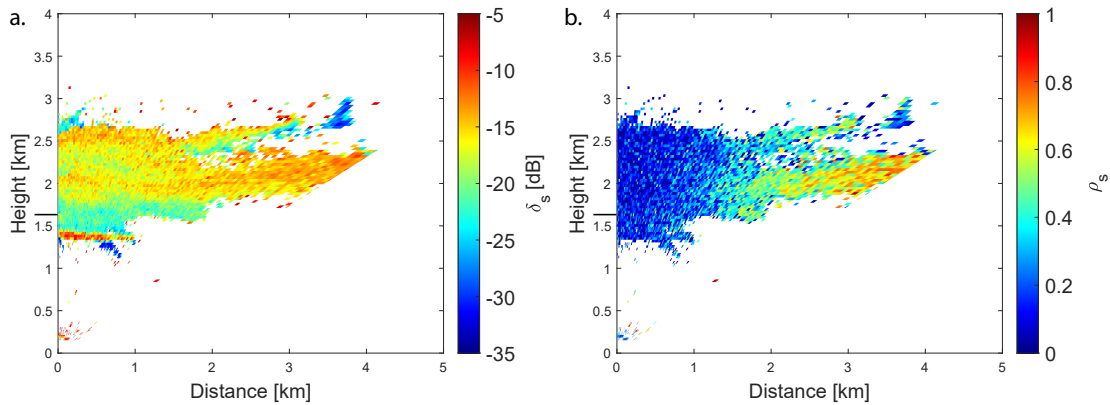


Figure 12. RHI-scan of (a) δ_s and (b) ρ_s on 4 January 2017, at 04:31 UTC in Limassol from 90° to 150° elevation angle. The black horizontal lines on the y axis mark the height of the analysed layer.

360 Figure 14 shows the vertical profile of ξ which confirms the dominance of prolate particles above the melting layer. The variability of ξ over the range from 1 to 2 is generally caused by the prolate shape of columnar crystals present within this cloud. From 2400 m to 1800 m height, the presence of columnar crystals with high axis ratio and/or high density such as compact needles is likely, as ξ in this layer exceeds 1.5. Accordingly, the Cloudnet classification, shown in Figure 11 (green box), classifies the hydrometeors as a mix of ice crystals and supercooled liquid droplets. The melting layer is located at
 365 around 1450 m height, where the transition between liquid droplets (red) and ice crystals (yellow) is visible in Figure 11. The temperature of the investigated case ranges from 0°C at the melting layer level and -10°C at the cloud top. This temperature range is characteristic for the formation of hydrometeors in the columnar particle shape class.

4.3 Oblate particle shape class: Dendritic ice crystals on 4 January 2017

The third case study aims on the description of oblate particles, such as dendritic crystals. The corresponding measurement
 370 was recorded in Limassol on 4 January 2017 at 01:30 UTC. The observed cloud system is marked by the blue frame in Figure 11. The observation was characterized by the presence of a relatively homogeneous liquid-topped ice cloud in the height range from 3200 m to 4200 m. Figures 15a and 15b show the RHI scans of δ_s and ρ_s , respectively. An increase of both δ_s and ρ_s from θ_{\min} to θ_{\max} , respectively, is visible. These gradients are particularly visible in Figure 16a which exemplarily shows the layer from 3300 m to 3331 m height, represented by the black line on the y-axis in Figure 15, where $\frac{\partial \delta_s}{\partial \theta} > \lim_{\delta_s}$ and $\frac{\partial \rho_s}{\partial \theta} > \lim_{\rho_s}$.
 375 ρ_s increases strongly from 90° to 110° elevation angle and levels off at 1 until θ_{\max} . $\delta_s(\theta_{\min})$ and $\delta_s(\theta_{\max})$ are calculated by as the mean of all data points contained in the 95% prediction interval of the polynomial fit represented by the dashed pink curves in Figure 16. According to Figure 6, the derived curve of ρ_s is typical of the polarimetric representation of the oblate particle class, as dendritic crystals. In Figure 16b, we see two intersections between $\hat{\delta}_s(\theta_{\min})$ and $\hat{\delta}_s(\theta_{\max})$. This configuration, associated with a positive gradient of both polarimetric parameters δ_s and ρ_s (table 2), implies to select the intersection at $\xi < 1$

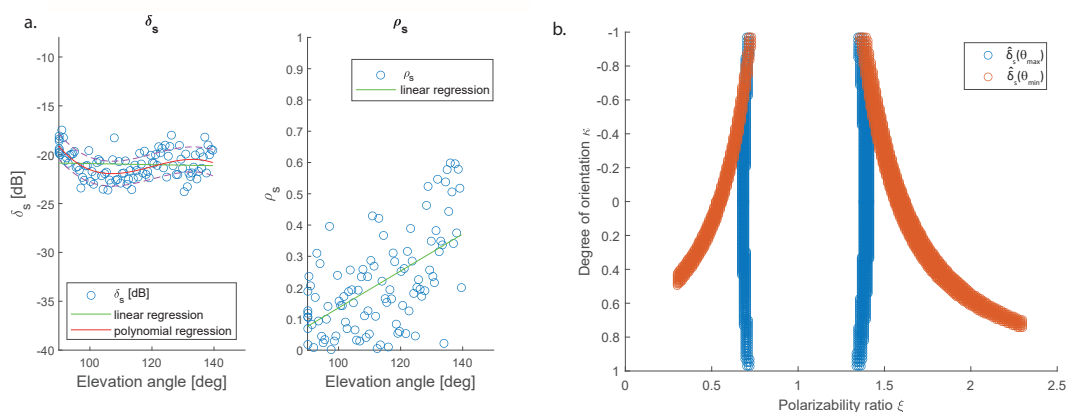


Figure 13. Detailed view into the columnar-shape case study presented in Figure 12 for the layer from 1617 m to 1648 m height. (a) Distribution of measured values of δ_s and ρ_s from θ_{\min} to θ_{\max} elevation angle and associated linear and polynomial fits. The dashed pink line in (a) corresponds to the 95% prediction interval from the third degrees polynomial function, used to determine the intersection of $\hat{\delta}_s(\theta_{\min})$ and $\hat{\delta}_s(\theta_{\max})$. (b) Intersection between $\hat{\delta}_s(\theta_{\min})$ and $\hat{\delta}_s(\theta_{\max})$ at θ_{\min} and θ_{\max} , respectively.

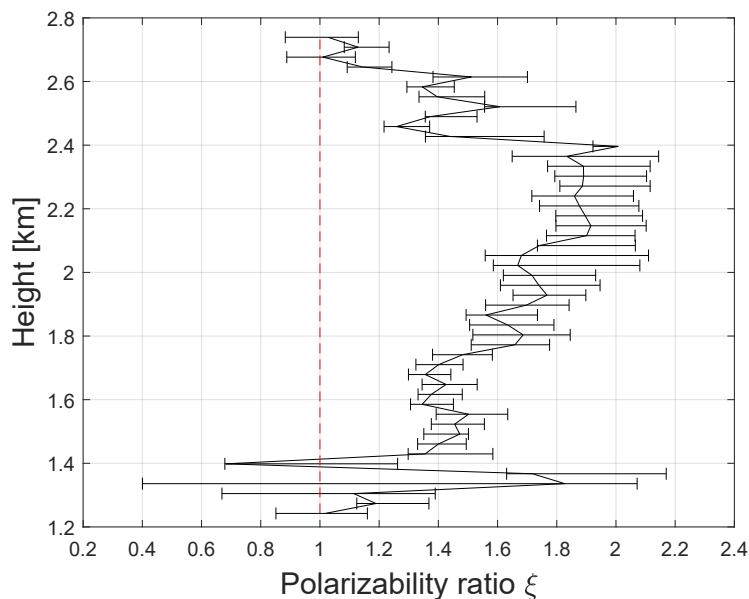


Figure 14. Polarizability ratio ξ calculated for each layer with the VDPS-method for the columnar-shape case study, observed at Limassol on 4 January 2017, at 04:31 UTC.

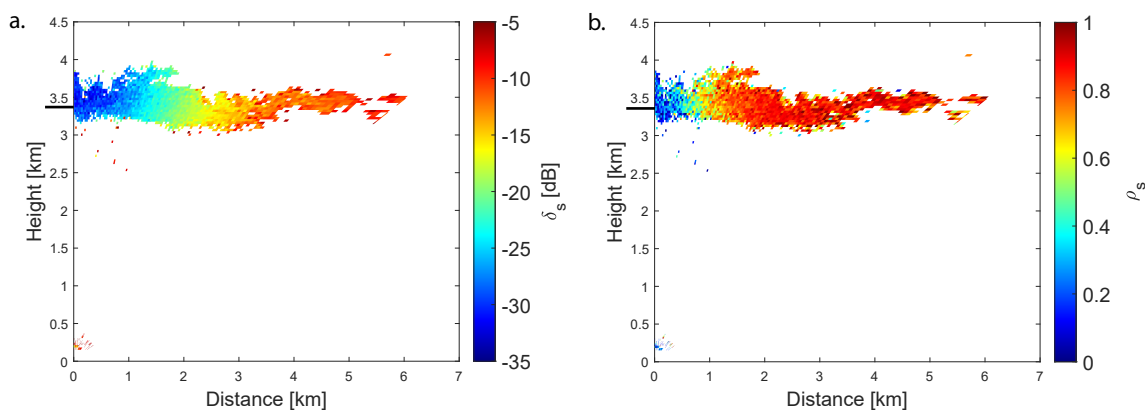


Figure 15. RHI-scan of (a) δ_s and (b) ρ_s on 4 January 2017, at 01:31 UTC in Limassol from 90° to 150° elevation angle. The black horizontal lines on the y axis mark the height of the analysed layer.

380 and $\kappa > 0.8$ for determination of the exact polarizability ratio, which corresponds to the oblate primary particle shape class. The vertical distribution of ξ presented in Figure 17 indicates $\xi < 1$ for all layers in the cloud. The values of ξ for this cloud is relatively constant between 0.3 and 0.5 which indicates that particles are strongly oblate and rather dense, which points likely to the class of dendritic crystals. In the Cloudnet classification shown in Figure 11, where the period of approximately 1 hour around the investigated RHI scan is indicated by the blue rectangle, ice crystals and contributions of supercooled liquid
385 droplets at cloud top where identified. The temperature in the cloud ranged from -15°C at cloud top to -10°C at cloud base. Laboratory studies suggest that, in this temperature range, the primary formation of dendritic ice crystals is most likely to occur (Bailey and Hallett, 2009). Hence, there is a remarkably good agreement between results of the VDPS method and observations for this case study, as well.

5 Discussion and conclusions

390 In this article, the Vertical-Distribution-of-Particle-Shape (VDPS) method was introduced. Based on earlier studies, which have succeeded in demonstrating the applicability of polarimetric parameters to estimate the particle shape (Matrosov et al., 2012; Myagkov et al., 2016a), this new approach aids one to characterize the shape of cloud particles from scanning SLDR-mode cloud radar observations. The 45° -slanted linear depolarization (SLDR) mode was chosen for the purpose of minimizing the influence of particle orientation by sedimentation, called wobbling effect (Matrosov et al., 2001), while providing well suited
395 and relatively easily observable input parameters for the shape retrieval. The VDPS approach represents a new, versatile way to study microphysical processes by combining a spheroidal scattering model (Myagkov et al., 2016b) applied only to $\hat{\delta}_s$, with real measurements of δ_s and ρ_s . In this paper, the VDPS method was introduced and validated by means of case studies collected in the frame of the CyCARE field campaign (Limassol, Cyprus), for three representative shape classes, oblate, isometric and

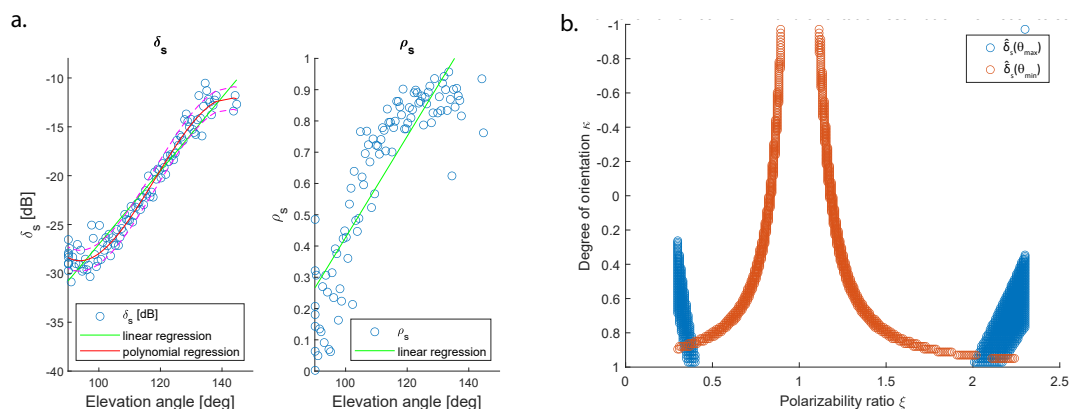


Figure 16. Detailed view into the dendritic-shape case study presented in Figure 8 for the layer from 3300 to 3331 m height. (a) Distribution of measured values of δ_s and ρ_s from θ_{\min} to θ_{\max} elevation angle and associated linear and polynomial fits. The dashed pink line in (a) corresponds to the 95% prediction interval from the third degrees polynomial function, used to determine the intersection of $\hat{\delta}_s(\theta_{\min})$ and $\hat{\delta}_s(\theta_{\max})$. (b) Intersection between $\hat{\delta}_s(\theta_{\min})$ and $\hat{\delta}_s(\theta_{\max})$ at θ_{\min} and θ_{\max} , respectively.

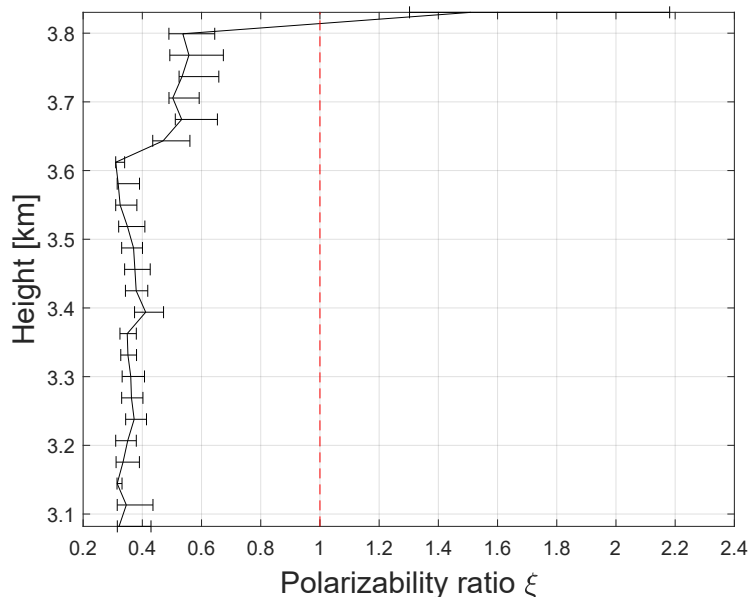


Figure 17. Polarizability ratio ξ calculated for each layer calculated with the new method for a dendritic-shape case study observed at Limassol, on 4 January 2017, at 01:31 UTC.



prolate particles, which present a polarizability ratio $\xi < 1$, $\xi = 1$ and $\xi > 1$, respectively. Before validating the VDPS method, the algorithm was tested and calibrated with success based on datasets from two field campaigns, CyCARE in Limassol, Cyprus, and DACAPO-PESO in Punta Arenas, Chile (Radenz et al., 2021) which sums up to three years of measurements at two different places.

The vertical distribution of the polarizability ratio ξ is precious because it informs about the transformation, sedimentation or stratification of hydrometeors in a cloud from top to bottom. Based on the information about the vertical distribution of particle shape in a cloud, the VDPS method provides valuable constraints for microphysical fingerprinting studies. The height-resolved view of the vertical distribution and evolution of particle shape in a cloud is helpful to study and characterize mixed-phase cloud processes in the onset phase of precipitation. While isometric, columnar and oblate particle shapes can well be distinguished with the VDPS method, discrimination between graupel (formed by riming) and aggregates (formed by aggregation) remains a challenge and is currently not possible solely with this method. Nevertheless, both processes can be identified based on the vertical evolution of ξ between cloud top and cloud base. In future, we therefore plan to associate the VDPS method with Doppler spectral methods in order to detect supercooled liquid droplets in mixed-phase clouds and to estimate the fall velocity of particles, which are relevant information to discriminate riming from aggregation. Indeed, riming processes require the presence of supercooled liquid droplets and the formed graupel are falling faster than aggregates because of their higher density (Kneifel et al., 2016; Vogl et al., 2022).

The VDPS method was implemented by means of an automatized framework, which permits us to obtain statistics about the particle shape for a long period of measurements and covering several field campaigns. Besides the mentioned strengths of the VDPS method, there are also certain limitations, which can eventually be overcome in future development steps. The first one is corresponding to the radar antenna quality, as it determines the calibration of δ_s and ρ_s . Polarimetric parameters δ_s and ρ_s are intrinsically dependent on the calibration of the antenna and the differential phase of the transceiver unit. Care must be taken to ensure a good calibration of the radar system. However, as was shown in this study, qualitative information about the elevation dependency of ρ_s is sufficient to identify the primary particle shape class when assuming horizontally oriented hydrometeors. For determination of the degree of orientation, the calibration of ρ_s needs to be improved so that it can be used quantitatively. In its current development state, the VDPS method is also only capable to investigate the shape of the main peak of the Doppler spectrum, as characterized by the highest peak of each Doppler spectrum obtained during an RHI scan at any given height level. The technique can thus not be used for evaluating the RHI scans for coexistence of several particle populations, as they might be superimposed by means of their differential fall velocities collected in a Doppler spectrum. Such peak separation techniques have already been developed for vertically pointing cloud radar measurements (Kalesse et al., 2019; Radenz et al., 2019) and will be adapted for scanning cloud radars in the near future.

Finally, our investigations have shown that applicability of the VDPS method is given even when measurements of δ_s are obtained only at two elevation angles θ_{\min} and θ_{\max} , which permits to change the duration of the required RHI scans as measurements at intermediate angles are not required any more, in contrast to the original approach of Myagkov et al. (2016b). This will considerably shorten the required amount of measurement time for each shape-retrieval measurement and improve the resolution of data points.



Code and data availability. The cloud-radar raw data and retrieval codes are available upon request. Please contact the first or second author.
435 Cloudnet data are available at <https://cloudnet.fmi.fi>. For plotting of the data, the tool pyLARDA, available at <https://github.com/lacros-tropos/larda>, was used.

Author contributions. AT developed the VDPS method, analysed the data and drafted the manuscript supervised by PS. JB conducted the CyCARE campaign and operated LACROS. PS, MR, and JB generated the Cloudnet datasets and supervised the data processing chain. AM supported me during the starting phase of the development work on the VDPS method and developed the spheroidal scattering model.

440 *Competing interests.* The contact author has declared that neither they nor their co-authors have any competing interests.

Acknowledgements. Development of the VDPS method was funded by the Deutsche Forschungsgemeinschaft (DFG – German Research Foundation) project PICNICC (SE2464/1-1 and KA4162/2-1). The authors wish to thank Cyprus University of Technology, Limassol, Cyprus, for their logistic and infrastructural support during the LACROS deployment. We gratefully acknowledge the ACTRIS Cloud Remote Sensing Unit for making the Cloudnet datasets publicly available. LACROS operations were supported by the European Union (EU)
445 Horizon 2020 (ACTRIS; grant no. 654109) and the Seventh Framework Programme (BACCHUS; grant no. 603445).



References

- Ansmann, A., Mamouri, R.-E., Hofer, J., Baars, H., Althausen, D., and Abdullaev, S. F.: Dust mass, cloud condensation nuclei, and ice-nucleating particle profiling with polarization lidar: updated POLIPHON conversion factors from global AERONET analysis, *Atmospheric Measurement Techniques*, 12, 4849–4865, <https://doi.org/10.5194/amt-12-4849-2019>, 2019.
- 450 Avramov, A. and Harrington, J. Y.: Influence of parameterized ice habit on simulated mixed phase Arctic clouds, *Journal of Geophysical Research: Atmospheres*, 115, <https://doi.org/https://doi.org/10.1029/2009JD012108>, 2010.
- Bailey, M. P. and Hallett, J.: A Comprehensive Habit Diagram for Atmospheric Ice Crystals: Confirmation from the Laboratory, AIRS II, and Other Field Studies, *Journal of the Atmospheric Sciences*, 66, 2888 – 2899, <https://doi.org/10.1175/2009JAS2883.1>, 2009.
- Bringi, V. and Chandrasekar, V.: *Polarimetric Doppler Weather Radar: Principles and Applications*,
455 <https://doi.org/10.1017/CBO9780511541094>, 2001.
- Bühl, J., Seifert, P., Myagkov, A., and Ansmann, A.: Measuring ice- and liquid-water properties in mixed-phase cloud layers at the Leipzig Cloudnet station, *Atmospheric Chemistry and Physics*, 16, 10 609–10 620, <https://doi.org/10.5194/acp-16-10609-2016>, 2016.
- Bühl, J., Seifert, P., Radenz, M., Baars, H., and Ansmann, A.: Ice crystal number concentration from lidar, cloud radar and radar wind profiler measurements, *Atmospheric Measurement Techniques*, 12, 6601–6617, <https://doi.org/10.5194/amt-12-6601-2019>, 2019.
- 460 Chandrasekar, V. and Keeler, R. J.: Antenna Pattern Analysis and Measurements for Multiparameter Radars, *Journal of Atmospheric and Oceanic Technology*, 10, 674 – 683, [https://doi.org/10.1175/1520-0426\(1993\)010<0674:APAAMF>2.0.CO;2](https://doi.org/10.1175/1520-0426(1993)010<0674:APAAMF>2.0.CO;2), 1993.
- Fan, J., Han, B., Varble, A., Morrison, H., North, K., Kollias, P., Chen, B., Dong, X., Giangrande, S. E., Khain, A., Lin, Y., Mansell, E., Milbrandt, J. A., Stenz, R., Thompson, G., and Wang, Y.: Cloud-resolving model intercomparison of an MC3E squall line case, *Journal of Geophysical Research: Atmospheres*, 122, 9351–9378, <https://doi.org/https://doi.org/10.1002/2017JD026622>, 2017.
- 465 Fukuta, N. and Takahashi, T.: The Growth of Atmospheric Ice Crystals: A Summary of Findings in Vertical Supercooled Cloud Tunnel Studies, *Journal of the Atmospheric Sciences*, 56, 1963 – 1979, [https://doi.org/10.1175/1520-0469\(1999\)056<1963:TGOAIC>2.0.CO;2](https://doi.org/10.1175/1520-0469(1999)056<1963:TGOAIC>2.0.CO;2), 1999.
- Görsdorf, U., Lehmann, V., Bauer-Pfundstein, M., Peters, G., Vavriv, D., Vinogradov, V., and Volkov, V.: A 35-GHz Polarimetric Doppler Radar for Long-Term Observations of Cloud Parameters Description of System and Data Processing, *Journal of Atmospheric and Oceanic*
470 *Technology*, 32, 675 – 690, <https://doi.org/10.1175/JTECH-D-14-00066.1>, 2015.
- Illingworth, A. J., Hogan, R. J., O'Connor, E., Bouniol, D., Brooks, M. E., Delanoé, J., Donovan, D. P., Eastment, J. D., Gaussiat, N., Goddard, J. W. F., Haefelin, M., Baltink, H. K., Krasnov, O. A., Pelon, J., Piriou, J.-M., Protat, A., Russchenberg, H. W. J., Seifert, A., Tompkins, A. M., van Zadelhoff, G.-J., Vinit, F., Willén, U., Wilson, D. R., and Wrench, C. L.: Cloudnet: Continuous Evaluation of Cloud Profiles in Seven Operational Models Using Ground-Based Observations, *Bulletin of the American Meteorological Society*, 88, 883 – 898,
475 <https://doi.org/10.1175/BAMS-88-6-883>, 2007.
- Kalesse, H., Vogl, T., Paduraru, C., and Luke, E.: Development and validation of a supervised machine learning radar Doppler spectra peak-finding algorithm, *Atmospheric Measurement Techniques*, 12, 4591–4617, <https://doi.org/10.5194/amt-12-4591-2019>, 2019.
- Kalesse-Los, H., Schimmel, W., Luke, E., and Seifert, P.: Evaluating cloud liquid detection against Cloudnet using cloud radar Doppler spectra in a pre-trained artificial neural network, *Atmospheric Measurement Techniques*, 15, 279–295, <https://doi.org/10.5194/amt-15-279-2022>, 2022.
- 480



- Kneifel, S., Kollias, P., Battaglia, A., Leinonen, J., Maahn, M., Kalesse, H., and Tridon, F.: First observations of triple-frequency radar Doppler spectra in snowfall: Interpretation and applications, *Geophysical Research Letters*, 43, 2225–2233, <https://doi.org/https://doi.org/10.1002/2015GL067618>, 2016.
- Korolev, A., Mcfarquhar, G., Field, P., Franklin, C., Lawson, P., Wang, Z., Williams, E., Abel, S., Axisa, D., Borrmann, S., Crosier, J.,
485 Fugal, J., Krämer, M., Lohmann, U., Schlenczek, O., and Wendisch, M.: Mixed-Phase Clouds: Progress and Challenges, *Meteorological Monographs*, 58, 5.1–5.50, <https://doi.org/10.1175/AMSMONOGRAPH-D-17-0001.1>, 2017.
- Matrosov, S., Mace, G., Marchand, R., Shupe, M., Hallar, A., and McCubbin, I.: Observations of Ice Crystal Habits with a Scanning Polarimetric W-Band Radar at Slant Linear Depolarization Ratio Mode, *Journal of Atmospheric and Oceanic Technology*, 29, 989–1008, <https://doi.org/10.1175/JTECH-D-11-00131.1>, 2012.
- 490 Matrosov, S. Y.: Prospects for the measurement of ice cloud particle shape and orientation with elliptically polarized radar signals, *Radio Science*, 26, 847–856, <https://doi.org/https://doi.org/10.1029/91RS00965>, 1991.
- Matrosov, S. Y., Reinking, R. F., Kropfli, R. A., Martner, B. E., and Bartram, B. W.: On the Use of Radar Depolarization Ratios for Estimating Shapes of Ice Hydrometeors in Winter Clouds, *Journal of Applied Meteorology*, 40, 479 – 490, [https://doi.org/10.1175/1520-0450\(2001\)040<0479:OTUORD>2.0.CO;2](https://doi.org/10.1175/1520-0450(2001)040<0479:OTUORD>2.0.CO;2), 2001.
- 495 Morrison, H., de Boer, G., Feingold, G., Harrington, J., Shupe, M. D., and Sulia, K.: Resilience of persistent Arctic mixed-phase clouds, *Nature Geoscience*, 5, 11–17, <https://doi.org/10.1038/ngeo1332>, 2012.
- Myagkov, A., Seifert, P., Bauer-Pfundstein, M., and Wandinger, U.: Cloud radar with hybrid mode towards estimation of shape and orientation of ice crystals, *Atmospheric Measurement Techniques*, 9, 469–489, <https://doi.org/10.5194/amt-9-469-2016>, 2016a.
- Myagkov, A., Seifert, P., Wandinger, U., Bühl, J., and Engelmann, R.: Relationship between temperature and apparent shape of pristine ice
500 crystals derived from polarimetric cloud radar observations during the ACCEPT campaign, *Atmospheric Measurement Techniques*, 9, 3739–3754, <https://doi.org/10.5194/amt-9-3739-2016>, 2016b.
- Radenz, M., Bühl, J., Seifert, P., Griesche, H., and Engelmann, R.: peakTree: a framework for structure-preserving radar Doppler spectra analysis, *Atmospheric Measurement Techniques*, 12, 4813–4828, <https://doi.org/10.5194/amt-12-4813-2019>, 2019.
- Radenz, M., Bühl, J., Seifert, P., Baars, H., Engelmann, R., Barja González, B., Mamouri, R.-E., Zamorano, F., and Ansmann, A.: Hemispheric contrasts in ice formation in stratiform mixed-phase clouds: Disentangling the role of aerosol and dynamics with ground-based
505 remote sensing, *Atmospheric Chemistry and Physics Discussions*, 2021, 1–34, <https://doi.org/10.5194/acp-2021-360>, 2021.
- Ryzhkov, A. V.: Interpretation of Polarimetric Radar Covariance Matrix for Meteorological Scatterers: Theoretical Analysis, *Journal of Atmospheric and Oceanic Technology*, 18, 315 – 328, [https://doi.org/10.1175/1520-0426\(2001\)018<0315:IOPRCM>2.0.CO;2](https://doi.org/10.1175/1520-0426(2001)018<0315:IOPRCM>2.0.CO;2), 2001.
- Schimmel, W., Kalesse-Los, H., Maahn, M., Vogl, T., Foth, A., Garfias, P. S., and Seifert, P.: Identifying cloud droplets beyond lidar attenuation from vertically pointing cloud radar observations using artificial neural networks, *Atmospheric Measurement Techniques*, 15,
510 5343–5366, <https://doi.org/10.5194/amt-15-5343-2022>, 2022.
- Solomon, A., de Boer, G., Creamean, J. M., McComiskey, A., Shupe, M. D., Maahn, M., and Cox, C.: The relative impact of cloud condensation nuclei and ice nucleating particle concentrations on phase partitioning in Arctic mixed-phase stratocumulus clouds, *Atmospheric Chemistry and Physics*, 18, 17 047–17 059, <https://doi.org/10.5194/acp-18-17047-2018>, 2018.
- 515 Vogl, T., Maahn, M., Kneifel, S., Schimmel, W., Moisseev, D., and Kalesse-Los, H.: Using artificial neural networks to predict riming from Doppler cloud radar observations, *Atmospheric Measurement Techniques*, 15, 365–381, <https://doi.org/10.5194/amt-15-365-2022>, 2022.